



# 1 3D Seismic Traveltime Tomography Validation of a Detailed 2 Subsurface Model: The case study of the Zancara River Basin 3 (Cuenca, Spain)

4  
5 David Marti<sup>1</sup>, Ignacio Marzan<sup>1</sup>, Jana Sachsenhausen<sup>1</sup>, Joaquina Alvarez-Marron<sup>1</sup>, Mario Ruiz<sup>1</sup>,  
6 Montse Torne<sup>1</sup>, Manuela Mendes<sup>2</sup> and Ramon Carbonell<sup>1</sup>  
7

8 <sup>1</sup> Institute of Earth Sciences Jaume Almera, ICTJA, CSIC, Lluís Solé I Sabaris s/n, 08028, Barcelona, Spain

9 <sup>2</sup> Department of Physics, Instituto Superior Técnico, IST, Av. Rovisco Pais, 1049-001 Lisbon, Portugal

10  
11 Correspondence to: David Marti [dmarti@ictja.csic.es](mailto:dmarti@ictja.csic.es)  
12  
13

## 14 ABSTRACT

15  
16 A high-resolution seismic tomography survey was acquired to obtain a full 3D P-wave seismic velocity image in the  
17 Zancara River Basin (east of Spain). The study area consists of lutites and gypsum from a Neogene sedimentary  
18 sequence. A regular and dense grid of 676 shots and 1200 receivers was used to image a 500x500 m area of the shallow  
19 subsurface. A 240-channel system and a seismic source consisting of an accelerated weight drop, were used in the  
20 acquisition. Half million traveltime picks were inverted to provide the 3D velocity model that allowed to resolve the  
21 structure up to 120 m depth. The project targeted the geometry of the underground structure with emphasis in defining  
22 the lithological contacts but also the presence of cavities and fault/fractures. An extensive drilling campaign provided  
23 uniquely tight constraints on the lithology; these included core samples and wireline-log geophysical measurements.  
24 The analysis of the well-log data enabled the accurate definition of the lithological boundaries and provided an estimate  
25 of the seismic velocity ranges associated to each lithology. The final joint interpreted image reveals a wedge shaped  
26 structure consisting of four different lithological units. This study features the necessary key elements to test the  
27 traveltime tomographic inversion approach in the high-resolution characterization of the shallow subsurface. In this  
28 methodological validation test, traveltime tomography demonstrates to be a powerful tool with a relatively high  
29 capacity for imaging in detail the lithological contrasts of evaporitic sequences located at very shallow depths, when  
30 integrated with additional geological and geophysical data.  
31

## 32 1. INTRODUCTION

33  
34 Knowledge of the very shallow structure of the Earth has become a critical demand for the modern society. The shallow  
35 subsurface is the part of the Earth with which humans have the most interaction. Characterizing the subsurface is  
36 important since it hosts critical natural resources; it is used as reservoir for resources and waste, plays a key role in  
37 support of infrastructure planning and holds the imprint of the anthropogenic processes. Thus, understanding its  
38 composition and structure is a regular objective in studies such as: natural resource exploration [Davis et al., 2003;  
39 Place et al, 2015] and environmental assessment studies [Steeple, 2001; Zelt et al, 2006]. It is also critical in civil  
40 engineering practice and monitoring of underground structures [Escuder-Viruet et al., 2003; Malehmir et al., 2007;  
41 Juhlin et al., 2007; Martí et al., 2008; Giese et al., 2009; Alcalde et al., 2013a]. In addition, the implementation of a  
42 competent subsurface exploration scheme is very valuable for assessing and/or providing detailed site characterization  
43 for addressing natural hazards, e.g., seismic hazard [Samyn et al. 2012; Ugalde et al., 2013; Wadas et al., 2017; Bernal  
44 et al., 2018]. Typical geotechnical practice for subsurface exploration has often relied on a combination of drilling, in  
45 situ testing, geophysical surveys, and laboratory analysis of field samples [Andara et al., 2011; Kazemeini et al., 2010;  
46 Alcalde et al., 2014].  
47

48 Geophysical techniques provide a great variety of approaches to accurately describe the structure, and the distribution of  
49 different physical properties in the subsurface. Depending on the target depth and the required spatial resolution  
50 different methodologies can be applied [e.g. Brys et al., 2018; Novitsky, et al., 2018; Malehmir et al., 2009 and 2011;  
51 Escuder-Viruet et al 2004; Carbonell et al., 2010; Ogaya et al., 2016; Andres et al. 2016, Alcalde et al., 2013b]. Since  
52 the late 90's sophisticated geophysical techniques have been developed to estimate near-surface velocity models as a  
53 proxy for subsurface stiffness in seismic applications with different targets [Bergman et al., 2004 and 2006; Heincke et



54 al., 2010]. Seismic traveltome tomography is a robust, efficient and well contrasted tool to constrain the rock's physical  
55 properties at very shallow depths [Yordkayhun et al., 2009b; Flecha et al., 2004; 2006; Marti et al., 2002a; ; Baumann-  
56 Wilke et al., 2012]. When seismic data is densely acquired it can provide very high spatial resolution images even in 3D  
57 at a much affordable cost than conventional 3D seismic reflection surveys. In areas where the geology has not  
58 particularly internal structural complexity and with moderate lateral lithological variability, traveltome tomography can  
59 provide a reliable image of the subsurface [Marti et al., 2002b; 2006; Yordkayhun et al., 2009a; Letort et al., 2012;  
60 Baumann-Wilke et al., 2012]

61  
62 The study area, in the Loranca Bainsin (Cuenca, Spain), has been considered as a possible host for a singular facility for  
63 temporary storage of radioactive waste. The emplacement of such a facility requires an extensive multi-scale, multi-  
64 disciplinary knowledge of the site's subsurface [Witherspoon et al., 1981; IAEA 2006; Kim et al, 2011], including a  
65 detailed 3D image of the structure and the distribution of its physical properties, specially focused on the upper hundred  
66 meters which directly interact with the ongoing construction works. The available data suggests that the sedimentary  
67 sequence in the study area presents certain tilting to the west, with no significant faulting and therefore no great  
68 structural complexity is expected in the shallow subsurface. Following similar case studies on very shallow site  
69 characterization, traveltome tomography was considered as the most adequate geophysical method to provide constraints  
70 on the seismic velocities for the 3D baseline model [Martí et al., 2002b; Juhlin et al., 2007; Yordkayhun et al., 2007].

71  
72 A very dense source-receiver grid was designed to assure the necessary lateral resolution and depth coverage of the  
73 seismic data, to constrain the geological features of interest beneath the construction site. The specific target was to  
74 resolve in detail the internal geometry of a mostly gypsiferous succession with diffuse lithological boundaries  
75 [Martinius et al., 2002; Diaz-Molina and Muñoz-García, 2010; Escavy et al., 2012;]. The inversion of almost half a  
76 million first arrival traveltome picks provided a 3D distribution of the P-wave velocities. This combined with borehole  
77 information allowed to fully characterize three main lithological units and constrain the interpretation of the velocity  
78 model. Borehole information was instrumental to define the specific 3D geometry of the different lithologies in the  
79 tomographic model and, the topography of the complex boundaries.

## 82 2. GEOLOGICAL SETTING

83  
84 The area of Villar de Cañas (Cuenca, Spain) is included in the Loranca Basin, in the southwestern branch of the Iberian  
85 Chain (Fig. 1a). The Iberian Chain corresponds to a wide mostly east-southeast trending Alpine intraplate orogen in the  
86 eastern Iberian Peninsula. . The structure consists of a thin-skinned, west-verging, mostly imbricate thrust system and  
87 associated fault-propagation folds that deform a Mesozoic and Cenozoic sedimentary cover detached above the  
88 Paleozoic basement [Muñoz-Martín y De Vicente, 1998; Sopenya y De Vicente, 2004]. The thrust faults merge at depth  
89 into a basal detachment located within Middle-Upper Triassic sequences [Piña-Varas et al, 2013].

90  
91 The crustal structure of the Iberian Chain has gathered academic interest since the early 1990's [see Seille et al, 2015;  
92 Guimerà et al., 2016 and references therein], including the acquisition of local and regional geologic and geophysical  
93 studies of the Loranca Basin [Biete et al., 2012; Piña-Varas et al., 2013]. The Loranca Basin comprises syntectonic  
94 Cenozoic strata [Guimerà et al., 2004]. It has been interpreted as a piggy-back basin that evolved during the Late  
95 Oligocene-Early Miocene period and includes mostly fluvial and lacustrine facies sediments, organized into three major  
96 alluvial fan sequences and their associated flooding plains (Diaz-Molina and Tortosa, 1996). The alluvial fans were fed  
97 from the southeastern and western boundaries of the basin and were comprised of mostly sandstones, gravels,  
98 mudstones, limestones and gypsum. Towards the center of the basin, in the most distal areas, mainly lakes, mud flats  
99 and salt-pans sedimentary facies associations developed. The evaporitic sequences targeted in this study were deposited  
100 in these distal sedimentary environments.

101  
102 The three large alluvial fans that build up the sedimentary infill of the Loranca Basin have been divided into three  
103 stratigraphic units named Lower, Upper, and Final Units (Figure 1). The Lower Unit was deposited during the Upper  
104 Eocene-Oligocene, during the initiation of thrusting along the Altomira Range. The Upper Unit includes mostly humid  
105 conditions, alluvial fan sedimentary facies at its base (Upper Oligocene-Lower Miocene), which have been described as  
106 the First Neogene Unit. Up until this period, the sedimentary sequences that are now isolated within the Loranca Basin  
107 were part of a much larger syntectonic Cenozoic basinal area in the center of Iberia, the Madrid Basin (Vegas et al.,  
108 1990; Alonso-Zarza et al., 2004; De Vicente and Muñoz-Martín, 2013). During sedimentation of the top of the Upper  
109 Unit, the Loranca basin became endorheic due to its disconnection from the Madrid Basin, related to the emergence of  
110 thrusts and formation of a topographic barrier along the Altomira Range (Diaz Molina and Tortosa, 1996). The  
111 endorheic sedimentary reorganization was associated with the establishment of much arid conditions in the region,  
112 during sedimentation of the Second Neogene Unit sequences. This unit includes four saline/evaporitic sequences



113 including saline clayey plains and marginal lacustrine environments, well developed in the central part of the Villar de  
114 Cañas Syncline, and that correspond to the area of our tomographic survey. The Final Unit of the Loranca Basin is not  
115 present within the Villar de Cañas Syncline.

116  
117 In the Villar de Cañas Syncline (Figure 1b), the Cenozoic sedimentary sequences are separated from each other by low  
118 angle unconformities. In particular, the outcropping Lower and Middle Miocene sediments of the Second Neogene Unit  
119 are surveyed by our study (Figure 1c). They are described as the Balanzas series, made up from bottom to top by the  
120 Balanzas Gypsum (Y) and the Balanzas Lower lutites (LT). The Y includes several types of gypsums alternating with  
121 lutites/shales that have been grouped in three units: i) macrocrystalline and laminated gypsums (Y1); ii) gypsum,  
122 shales/lutites and marls (Y2); and iii) gypsum with shaly-marly levels and gypseous alabaster (Ytr) (Figure 1). The LT  
123 crops out in the core of the Villar de Cañas syncline and contains red siltstones and mudstones with some gypsum  
124 and/or sands (Figure 1).

125  
126 According to the Second Neogene Unit sequence, gypsum rocks are the main lithological target in the study area. The  
127 definition of their internal structure and the boundaries between the different sequences are often difficult, considering  
128 the heterogeneity of these deposits. Gypsum ( $\text{CaSO}_4 \cdot 2\text{H}_2\text{O}$ ) is frequently affected by diagenetic processes and, as a  
129 consequence, gypsum rocks include clay, carbonates and other minerals. The presence of other minerals affects the  
130 purity of the gypsum rocks and this is reflected in changes of its physical properties potentially measurable with  
131 geophysical methods [Carmichael, 1989; Guinea et al., 2010; Festa et al, 2016]. However, their variability in  
132 composition and their complex geometry make the characterization of these deposits challenging [Martinius et al.,  
133 2002; Diaz-Molina and Muñoz-Garcia, 2010; Escavy et al., 2012; Kaufman and Romanov, 2017]. In this case, the  
134 high-resolution seismic characterization of the site was designed taking into account all these structural and lithological  
135 constraints.

136

### 137 3. DATA ACQUISITION AND PROCESSING

138

139 To provide a detailed image of the target site shallow subsurface, we designed a dense 3D tomographic survey to ensure  
140 a high spatial resolution. The approximately regular acquisition grid covered an area of 500x500m. Source locations  
141 were distributed in a grid of 20x20 m cells. Receivers were distributed along profiles oriented east-west, with 20m  
142 spacing. Along each line, 48 receivers were distributed with a receiver spacing of 10 m (Figure 2). The seismic source  
143 consisted in a 250 kg accelerated weight drop. The seismic data acquisition system consisted in ten 24 channel GEODE  
144 ultra-light seismic recorders (Geometrics systems) that resulted in a 240-channel system. Each channel included a  
145 conventional vertical component geophone. With the available instrumentation, the acquisition scheme required 5  
146 swaths to cover the entire study area. Each swath consisted in five active receiver lines (240 channels), a total of 676  
147 source shot positions resulting in a total of 3380 shot gathers. The survey was acquired and completed in two different  
148 time periods (December 2013 and January 2014). The acquisition program was carefully adapted to account for the  
149 special circumstances associated to the acquisition of different swath at different times, with different environmental  
150 conditions (e.g. different level of ambient noise, weather changes, or potential technical problems in acquisition  
151 equipment). One of the main concerns was to ensure the release of enough acoustic energy for all the available offsets,  
152 especially in presence of complicated weather conditions. The 250 kg accelerated weight drop source ensured high  
153 signal-to-noise (S/N) ratios in most of the shot points (Figure 3). However, some of them required repetition of the shot  
154 to improve the S/N ratio by means of raw data stacking. Despite the complexity of the seismic acquisition, the recorded  
155 seismic data was of high quality and high S/N ratio and allowed a well-defined picking of first arrivals (Figure 3)  
156 corresponding to almost all the offset range, reaching maximum offsets of almost 700 m. The high quality of the seismic  
157 first arrivals favored the semi-automatic picking of more than a half million of first breaks.

158

159 The algorithm used with this data (Pstomo\_eq) is a fully 3D traveltimes tomographic inversion code [Benz et al., 1996;  
160 Tryggvason et al 2002]. The forward modeling is a first-order finite-difference approximation of the eikonal equation,  
161 computing all the time field from a source (or receiver) to all the cells of the model (two different schemes are available  
162 based on Hole and Zelt, [1995] and Tryggvason and Bergman, [2006]). The traveltimes to all receiver or source  
163 positions are computed from the resulting time field and raytracing is performed backwards, perpendicular to the  
164 isochrons [Vidale, 1998; Hole 1992]. The inversion is performed with the conjugate gradient solver LSQR [Paige and  
165 Saunders, 1982]. One of the main requirements for a successful inversion is the selection of an appropriate initial model  
166 [Kissling, 1988; 1994]. A good approximation to the minimum starting model is the use of the *a priori* information  
167 available for the area, based on the surface geology and/or the geophysical data previously acquired. In our case, an  
168 initial 1D model was built based on the sonic log information available for different boreholes located within the study  
169 area (Figure 2). The shallow target of the tomographic experiment and the well-controlled sedimentary sequence  
170 expected at these depths, with a non-complex laterally changing geology, favored the election of very suitable initial  
171 models.



172

173 The particular acquisition pattern carried out in different swaths forced to establish a careful quality control over the  
174 data. These factors may introduce some bias to the first arrivals picks (Figure 3) that could affect the convergence of the  
175 inversion algorithm. To avoid any potential error associated to the different conditions during the acquisition we decided  
176 to invert all the swaths independently to check the data quality and their convergence. Once convergence was tested in  
177 every swath, the other swaths were gradually added into the inversion. This resulted in a relevant improvement on the  
178 lateral resolution and a better definition of the final velocity model. The inversion of single swaths was also used to test  
179 the dependence of the result on the choice of initial models. Different initial 1D velocity models based on the previous  
180 geophysical and geological information were built to analyse the consistency with the first break picks and the  
181 robustness of the inversion. The best fitting 1D model chosen provided an RMS reduction of 93% showing a clear 2D  
182 trending geometry in the east-west direction. Taking into account this feature, that was also observed in the surface  
183 geology (Figure 1 and, 2), as well as the borehole information, an initial 2D velocity model was built. This initial  
184 model was then used to speed up the convergence of the calculations and to reduce the number of iterations needed to  
185 reach the optimal final RMS misfit.

186

187 The inversion cell size decreased during the integration of the first arrival picks corresponding to the different swaths.  
188 Due to the sparse distribution of receivers in the north-south direction the cell size corresponding to this direction was  
189 the most sensitive to the addition of new traveltimes picks to the inversion. Obviously, the reduction of the inversion cell  
190 size was also relevant to increase the resolution of the final velocity model, resulting in a final inversion grid spacing of  
191 10x20x5 m (for x, y and z).

192

#### 193 4. RESULTS

194

195 The inverted final velocity model shows a detailed image of the shallow subsurface of the study area (Figure 4). This  
196 model provides the best fitting result featuring a final RMS traveltimes residual of 2.5 ms, which is indicative of the  
197 good convergence of the inversion process. According to the raypath coverage obtained during the inversion, the  
198 velocity model retrieves the internal structure of the subsurface with a maximum depth of 120 m (Figure 4), especially  
199 in the central and western sector of the survey. This recovering depth decreases drastically towards the east. This was  
200 partly due to the usual ray coverage decrease close to the boundaries of the survey but also to other different causes. The  
201 lateral changes in surface geology in this sector affected seismic source coupling reducing the overall energy injected in  
202 the subsurface and affecting the seismic source repeatability. This issue hindered the identification of the first arrivals in  
203 a wide range of offsets for the shot points located in the eastern part of the study area (Figure 4). Furthermore, the high  
204 velocity gradient observed at very shallow surface also affects the depth of the traced ray paths.

205

206 The direct observation of the 3D P-wave velocity model reveals several interesting features about the shallow  
207 subsurface and its internal structure. The tomographic model shows that the shallowest subsurface (first 5-10 m) is  
208 characterized by a very low seismic velocity. This upper layer seems to have a relatively constant depth for the entire  
209 study area. Beneath, there is a velocity gradient smoother towards the northwest, slightly increasing to the south and  
210 significantly to the east (Figure 4). This effect is remarkable in the northeast corner of the study area, where the velocity  
211 rise from 1000-1200 m/s in the shallow surface to up 4000-4500 m/s in the first 20-30 m (Figure 4). This results in a  
212 wedge geometry of the velocity model, indicating a clear northwest dipping trend of the main structural features.  
213 Another significant result is the lateral changes in velocity observed in the deepest part of the model which could  
214 suggest the presence of lateral lithological changes..

215

216 Different checkerboard tests were carried out to estimate the potential resolution of the final velocity models obtained  
217 in the tomographic inversion (Figure 5). These sensitivity tests provide a qualitative estimation of the spatial and depth  
218 resolution and the uncertainty of the experimental design used. The main idea is to test how well the acquisition  
219 geometry (distribution of sources and receivers) is able to recover a regular distribution of velocity anomalies.  
220 Checkerboard tests only provide indirect evidence of these measures [Lévéque et al., 1993; Rawlinson et al., 2016].  
221 These tests illustrate where, or what parts of the subsurface models are best resolved. The information that these tests  
222 reveal is similar to the resolution and covariance matrix measures obtained by other conventional schemes. For  
223 example, covariance matrix methods in LSQR [Yao et al., 1999] give incomplete information, especially when sources  
224 and receivers are located at surface. In this case, the raypaths are strongly dependent upon the velocity gradient which  
225 implies a significant non-linearity [Bergman et al., 2004; 2006]. Keeping that in mind, several tests, including using  
226 different size of the anomalies, were applied to our data. Two different sections, one east-west and one depth slice,  
227 representative of the complexity of the study area, have been selected to illustrate the results of the checkerboard  
228 analysis (Fig. 5). First of all, an east-west section located at the center part of the tomographic 3D volume shows that  
229 the velocity anomalies are retrieved for the first 100 m in almost all the study area, slightly reducing its depth of



230 penetration close to the eastern sector. This fact was expected, due to the lower quality of the first arrivals of the shots  
231 located in this area. The traveltimes picking carried out in this area were very limited in offset, which clearly impeded to  
232 reach deeper exploration depths. On the other hand, a section at constant depth shows a very homogeneous distribution  
233 of the anomalies recovered of the checkerboard test. At 45-50 m depth the resolution analysis assures that the ray  
234 coverage is homogeneous and well distributed throughout the entire surface. The least covered area corresponds to the  
235 north and the southwest part. Although these areas correspond to the boundaries of the study areas, where lower  
236 resolution is expected, technical problems with the geophone cables forced us to disconnect 24 of the 48 channels in the  
237 northernmost receiver line and 12 channels in the southwestern sector in four receiver lines in a row. In spite of these  
238 acquisition issues, the checkerboard analysis demonstrates the capability of our experimental system/device to image  
239 with sufficient detail the shallow subsurface.  
240

#### 241 4.1 Velocity model interpretation

242  
243 Despite the velocity model provides a detailed image of the shallow subsurface, a direct geological interpretation is  
244 difficult, especially in terms of structural features. Interval velocities from sonic logs are critical for a realistic  
245 interpretation of the 3D tomographic model so that the internal structure of the shallow subsurface can be geologically  
246 inferred.  
247

248 As mentioned above, the study area was covered by an extensive borehole drilling campaign (including geotechnical  
249 and geophysical boreholes with core sampling) and a very detailed surface geology mapping which provided the  
250 necessary information to properly decode the geological meaning of the P-wave velocity model. Within the study area  
251 only four geophysical equipped wells were available, and used to guide the interpretation of the velocity model  
252 (boreholes: SG-29, SG-30, SG-28 and SVC-6, shown in Figure 6). The sonic logs, the tailings and the core samples  
253 were critical in linking the different lithologies to the geophysical responses. The lithology and the tomographic image  
254 were linked by correlating the velocity profiles obtained from the tomographic model with those determined from the  
255 sonic logs. This correlation required a homogenization so that the scales of resolution of both methods would be  
256 comparable. The 3D tomographic images are built as velocity grids with cell dimensions of 10x20x5m (x, y, z). This  
257 indicates that the sampling interval in the vertical (z) direction is 5 m, while the sample rate in the z axis of the logs is  
258 on the cm scale. Thus, the V<sub>p</sub> logs needed to be re-sampled to provide average interval velocities in 5 m intervals,  
259 representative of the average lithology within this interval. Two resampling approaches were tested. First the log was  
260 averaged using a 5 m averaging window, and then re-sampled in 5 m intervals (Figure 4); window lengths from 2.5 to  
261 10 m were also tested, but provided similar results. A median filter approach, that avoids extreme values, was also  
262 evaluated, providing a similar response, so the 5m interval average method was finally selected. This homogenization  
263 step assured that scale-lengths of the features observed in both data sets were comparable.  
264

265 The information derived from the well logs provided constraints to interpret up to nine lithological sub-units (Figure 6).  
266 However, the relatively reduced overall depth coverage of the tomographic image makes that only four of these units  
267 may be identified in the velocity model (Figure 4, and 6). Characteristic lower and upper limits as well as average  
268 seismic propagation velocities for P-waves were estimated for each different lithological unit using the sonic log  
269 measurements, resulting in the table scale shown in Figure 6.  
270

271 The gamma ray logs are the most complete logs in the available boreholes, which makes them crucial to define the first  
272 lithological boundary at depth (Figure 6). The velocity data is sparser than the gamma ray data, and only the borehole  
273 SVC-6, located in the center part of the study area (Fig. 2), provides an almost complete velocity log as a result of the  
274 combination of the downhole data and the sonic log. The analysis of the well data differentiates a first upper layer that  
275 according to the core samples corresponds to the Balanzas Lower lutites (LT). This sedimentary rock consists mostly of  
276 clay minerals with large openings in their crystal structures, in which K, Th and U fit well. This fact makes the gamma  
277 ray measurements ideal for its identification because they are very sensitive to the presence of natural radioactivity. A  
278 sudden decrease of the gamma ray values clearly defines the transition to a new lithology (Figure 6). The direct  
279 observation of the SVC-6 velocity log shows two well distinguished sections characterized by different seismic  
280 velocities. The recorded values are relatively low (< 2000 m/s) for the first 10-12 m, with a sudden increase at this depth  
281 up to 2200m/s, keeping this velocity relatively constant until the transition zone (~24 m) (Figure 6). The boundary with  
282 the deeper formations is observed in V<sub>p</sub> with an gradual increase in the velocity values close to 3000 m/s, that takes  
283 place in a few meters indicating a smooth transition in terms of velocities. From the log analysis it can also be derived  
284 that the thickness of the LT layer is almost constant in north-south direction in the central part of the study area (around  
285 20 m depth in SG-28, SG-30 and SVC-6)), increasing its thickness to 32 m in the western sector in which SG-29 is  
286 located. The lack of logging information in the Eastern part of the study area forces the interpretation to rely solely on  
287 the information from the surface geology (Figure 2) The geological map shows the presence of this lithological  
288 interface located in the eastern sector of the study area, with an approximate orientation N-S being suddenly moved to the



289 West in the middle part of the study area. This interface puts in contact the lutites layer with the next lithology identified  
290 in the core samples. This fact suggests that the layers dip gently to the West supporting the wedge geometry observed in  
291 the tomographic model and following the regional scale geologic interpretations [Biete et al 2012; Piña-Varas et al.,  
292 2013].

293  
294 Just beneath the LT layer, the core samples show the presence of a gypsum-lutite transition layer of nearly constant  
295 thickness in most of the study area (at least where the logging information is available) with a local increase in  
296 thickness in the Western sector. This unit, called Ytr, belongs to the Second Neogene unit and is characterized by  
297 mainly gypsum with centimetric to metric intercalations of shaly/marly levels. These lithological changes are  
298 characterized by a high variability in the recorded sonic and gamma ray log values. The presence of these gypsiferous  
299 shales are clearly observed in the gamma ray logs, featuring high peaks related to the shaly intercalations. In the sonic  
300 logs, the velocity seems to increase in the upper part of the unit with a decrease that coincides with higher presence of  
301 the shaly-marly levels (increase in the gamma ray log): Close to the transition to the next lithology, the sonic log seems  
302 to recover the velocity values observed in the upper part.

303  
304 A great increase in the velocity together with a sudden decrease in the gamma ray values indicates the transition to a  
305 thick lithological sequence of gypsum in depth. In terms of borehole logging several subunits can be inferred according  
306 to the different signatures observed. However only two of these gypsum units, defined in the geological setting, can be  
307 observed/correlated in the tomographic model taking into account the depth achieved with the acquisition geometry  
308 used. The upper unit (Y1) is defined by higher values of seismic velocities (~4250m/s) than the deeper unit (Y2)  
309 (~3800m/s).

310  
311 The identification of the main lithological units by means of the logging data and the core samples provides a solid link  
312 between the geology and the physical properties that allow us to lay out a structural interpretation the 3D tomographic  
313 volume. The standard deviation of every averaged velocity value was used to estimate a rough velocity range  
314 corresponding to each lithology but also provided a measure of the quality of the assigned velocity to the different  
315 lithologies. This criterion was then used to correlate each P-wave velocity value of the mesh to the defined lithologies  
316 (Figure 7). Looking at the velocities table, the LT layer seems to be the most well-established value, according to the  
317 standard deviation obtained, which is the lowest (90 m/s). Nevertheless, that this layer was defined only by using the  
318 deeper portion of the log data corresponding to this section, which probably corresponds to the higher velocities for this  
319 formation neglecting the low values that should be expected at shallow depths due to weathering, unconsolidation etc.  
320 which will significantly increase the standard deviation. This is the case of the Ytr layer which features a standard  
321 deviation of 400 m/s which clearly reflects the high variability of the seismic velocities observed in the sonic logs.

322  
323 This velocity analysis allowed us to re-image the tomographic velocity model, this time assigning the different  
324 lithologies to the assigned velocity ranges observed in the well log data (Figure 7 and 8). In this way, we could map the  
325 four lithological units within the velocity model, clearly defining their respective boundaries and other structural  
326 features which characterize the shallow subsurface of the test site.

327

## 328 5. DISCUSSION

329

330 The direct observation of the different lithological domains identified in the guided interpretation reveals several  
331 interesting general features (Figure 8). The defined upper boundaries feature an undulating character that reveals  
332 channel-like structures with an east-west orientation. Note that the sedimentary environment during Upper Oligocene-  
333 Lower Miocene was meander set up [Diaz-Molina, 1993]. Furthermore, the LT and the Ytr layers appear to increase  
334 their thickness towards the west keeping it constant in the north-south direction (Figure 7, 8 and 9) which indicates that  
335 the gypsum layers are dipping towards the west. This coincides with the wedge geometry clearly observed in the  
336 tomographic velocity models (Figure 4 and 7). The latter was also suggested by the regional scale geology and other  
337 geophysical studies [Biete et al., 2012; Piña-Varas et al., 2013].

338

339 In order to validate the accuracy of the logging guided interpretation of the tomographic model, several 2D velocity  
340 sections in depth were extracted following different existing east-west and north-south geological profiles. Those  
341 selected profiles corresponds to geological cross-sections based on data collected at surface and the interpretation of the  
342 core samples. Besides, the interpreted boreholes used in this study were also projected to the closest profiles, thus  
343 providing additional information to compare and evaluate the final structural interpretation of the 3D velocity grid.

344

345 The definition of the different lithological boundaries was one of the main objectives of this study. In this sense, the  
346 resulting images show a general good agreement between the geological cross-sections, the interpreted boreholes and



347 the tomographic models, in terms of boundary definitions, geometry and depth throughout all the 3D volume (Figure 9).  
348 The matching between hard data (surface geology plus well-log data) and soft data (seismic tomography) is very  
349 consistent taking into account the different criteria used and resolution to define the lithological changes in depth. The  
350 correlation between both interpretations is particularly significant in the central part of the study area, where the  
351 lithological boundaries defined in the geological cross-sections even show changes in dip and undulating geometries  
352 also retrieved by the seismic velocity models. In those areas, the comparison between the interpreted boreholes  
353 projected to the velocity profiles is also in good agreement (Figure 9). Nevertheless several discrepancies are observed  
354 in specific areas, specially located on western and eastern ends, affecting to different lithological layers, which need to  
355 be addressed in detail to finally validate the tomographic models.  
356

357 From depth to surface the first units identified are Y1 and Y2 (Figure 8). From the previous geological analysis, this  
358 gypsum units are characterized by a complex internal structure with no clear defined boundary, continuous lateral  
359 changes and the presence of widely disperse massive gypsum bodies. The tomographic model seems to corroborate this  
360 by showing a quite complex distribution of these two units in the 3D velocity volume. Unfortunately, the depth  
361 resolution of the tomographic model together with the velocity inversion observed between the Y1 and Y2 (Figure 4)  
362 makes very difficult to provide a reliable retrieval of the seismic velocities associated to each lithology. This issue is  
363 well described in the literature, such as in the one described in Flecha et al. (2004). These aspects together with the  
364 smooth character of the seismic tomography leads to consider these gypsum units as a unique lithology, focusing in the  
365 upper boundary definition and avoiding the definition of the complex internal structure. Besides, this objective was  
366 beyond the scope of the study and from an engineering point of view, both lithological units can be considered as one  
367 unit in terms of mechanical response.  
368

369 The upper limit between Y1+Y2 (Y) and Ytr is relatively well constrained in almost all the area, especially when  
370 compared with the log interpretation. Changes in dip and variable geometries in depth observed in the geological cross-  
371 sections are also imaged by the guided interpretation of the 3D velocity model (Figure 9). The well contrasted seismic  
372 velocities between both lithologies observed in the well logs help in the boundary definition, although the previously  
373 mentioned limitations of seismic tomography for these lithologies makes impossible to reach the seismic velocity  
374 ranges expected for the gypsum units according to the logging data (Figure 4). The tomography velocity model suggests  
375 the velocity inversion in some of the profiles (i.e. profile c9i in Figure 9). The tentative interpretation of the Y1  
376 (Gypsum 1 in Figure 8) clearly does not correspond to this lithology which should be the unit defining the upper  
377 boundary of this gypsum sequence; however it is presented in the results because is indicative of the presence of these  
378 isolated massive gypsum bodies that are observed and well defined especially in the eastern sector of the study area,  
379 some of them very close to the surface.  
380

381 Quite different is the LT-Ytr boundary definition which seems to be underestimated in depth location as we move to the  
382 western sector of the survey area (Figure 9). Several considerations can be taken into account to understand this  
383 mismatch observed between different interpretations. First, this lithological boundary is relatively diffuse because of the  
384 presence of the gypsiferous lutites as intercalations distributed within the gypsum rock. This fact is the cause of the  
385 appearance of peaks of higher velocity in the sonic logs which are responsible for the increase in the average velocity  
386 for the Ytr unit. Unfortunately, due to the acquisition geometry, the resolution that characterizes the tomographic model  
387 is not able to differentiate between these intercalations/interfingering (lenticular shape layers of centrimetric to metric  
388 scale) within Ytr which would have helped to define this boundary in greater detail. As mentioned above, we resampled  
389 the velocities from sonic logs to correlate their velocities to the tomography results. As a result, the averaged velocity  
390 associated to Ytr is characterized with a high standard deviation (Figure 6 and 8). This increases the uncertainty of Ytr  
391 identification in the whole tomographic 3D volume which induces some mismatch in the unit identification.  
392

393 On the other hand, the location of the boreholes used for the guided interpretation of the tomographic model also can  
394 account for these observed discrepancies. Most of them (SG-28, SVC-6 and SG-30) are located in the central part of the  
395 study area and besides they are aligned in the north-south direction. Thus, the weight of these three boreholes in the  
396 estimation of the velocity intervals in both lithologies involved is significant and introduces a bias for the rest of the  
397 tomography guided interpretation. According to these wells, the lutites have a quite similar thickness placing the  
398 lithological boundary at a relatively shallow depth (around 20 m) compared with the same boundary in the western area  
399 which is located at a deeper level. This implies that the velocity derived from the boreholes for the LT layer is most  
400 probably underestimated in relation to the expected velocities for this lithology at this part of the survey. The effects of  
401 the soil compaction, due to the layer thickening in this sector, could increase the velocity of the lutites at depth. This  
402 fact but also the standard deviation associated to the Ytr unit seems to be a strong effect in the delimitation of this upper  
403 boundary when moving to the west. Both factors lead to a mismatch between the different interpretations. This can be  
404 observed in the velocity sections presented in Figure 9. In the east-west velocity sections there is also a similar effect,  
405 although showing a better match between geological and tomographic delineation of this boundary as we move  
406 eastward. The north-south sections show definitive evidence of this. Profile c-9i presents a good agreement between



407 both interpretations, note that this profile is practically aligned with boreholes SG-28, SVC-6 and SG-30. Conversely,  
408 section c-8i shows a clear discrepancy since it is located further to the west in relation to the c-9i profile.

409  
410 The tomographic velocity model suggests the presence of a shallow weathered layer (warm colors in Figure 4). This  
411 layer is clearly observed on the field, the surface mapping and the core samples recovered in most of the geotechnical  
412 boreholes. These observations show that this very shallow layer have two different lithologies that correspond to lutites  
413 (LT) at the northern and western sector of the study area and also transition gypsum (Ytr) in the eastern sector (Figure 2  
414 and 6). This upper weathered layer seems to be characterized by low velocity values though, from a seismic velocity  
415 point of view, both lithologies are barely distinguishable. Furthermore, the guided interpretation of the tomographic  
416 model is also unable to retrieve this layer basically due to the incompleteness of the sonic logs at shallow depths (only  
417 downhole data in available for SVC-6) (Figure 6). This is specially significant for the weathered Ytr unit which has no  
418 recorded data to estimate its seismic velocity at shallow surface. For this reason, in the guided interpretation this  
419 identified weathered layer has not been considered as a differentiated boundary. However, the surface geology offers a  
420 perfect way to define the boundary associated between both lithologies in this upper weathered layer. Methodologically  
421 it indicates that the direct mapping/correlation between velocity and lithology might not be applicable when the  
422 influence of other factors is relevant. Weathering affects the physical properties of the lithology that is outcropping,  
423 decreasing velocities characteristic of the Ytr to values below 2100 m/s, the upper limit criteria used to identify the LT.

424  
425 The imaging of the LT-Ytr transition cannot be accomplished using only the tomographic velocity model, according to  
426 the borehole logging data available. More borehole logging data in representative locations of the velocity model are  
427 needed to better constraint the velocity range assigned to each lithology, which in turn would enable to improve the  
428 velocity ranges and reducing the standard deviations for each unit. A complete sequence for the sonic logs, from surface  
429 to the maximum depth, will be very useful to further constraint the weathered layer and maybe it could offer a clue to  
430 differentiate at surface lutites from gypsum from a seismic velocity point of view. Nevertheless, seismic velocity alone  
431 seems to have some limitations to clearly define both lithologies or at least there is no a clear and unique distinctive  
432 signature for these two lithologies. For this reason, we believed that adding other physical properties (e.g. resistivity or  
433 porosity) could improve the definition of the LT-Ytr transition.

434  
435 One of the main concerns is the presence of dissolution cavities within the evaporitic sequence, especially taking into  
436 account the possible host of a singular infrastructure. In this sense, travelttime tomography is very limited in recovering  
437 the location, geometry and velocity values expected for a cavity. Besides this is particularly more difficult if only  
438 surface seismic data are used in the inversion (Flecha et al., 2004). In case of the presence of a cavity, the wavefront do  
439 not propagate through it and the first arrivals are only capable to record the perturbation due to the large velocity  
440 contrast at the edge of the velocity anomaly. Fortunately, the density ray diagrams revealed as an appropriate tool to  
441 define the presence of cavities which is characterized by a very low or a lack of ray coverage. Taking into account this,  
442 the analysis of the ray coverage diagrams derived from the travelttime inversion do not show any evidence of this fact  
443 which implies that no cavities are characterized, at least at decametric scale (Figure 4, 5 and 7). Furthermore, the  
444 extensive borehole campaign carried out on site also showed no evidence of the presence of cavities in the shallow  
445 subsurface.

446  
447 On the other hand, the presence of potentially active faults in the area is also a main issue in hazard analysis and risk  
448 assessment. For this reason, the study of the presence of any non mapped minor fault and the characterization in depth  
449 of mapped ones was also of interest. The study of instrumental and historical seismicity showed that the area was  
450 tectonically stable with a very reduced amount of seismic events in the area and of very low magnitude. Furthermore  
451 the paleoseismic studies by means of trenches revealed that does not exist any evidence of recent seismic activity  
452 related to any fault system. In the same way, the analysis of the tomographic velocity model supports these statements  
453 about evidences of recent faulting responsible of any seismic activity that it could constitute any risk. The lithological  
454 units imaged by the velocity models no not show any evidence of faulting which indicates that this sedimentary package  
455 has not been affected by any recent activity (Figure 7, 8 and 9). This fact supports the evidences showed by other  
456 studies carried out in the area.

457

458

459

460

461

462

463

464

465

466

467

468

469

470

471

## 6. CONCLUSIONS

461 The detailed 3D structure of an evaporite sequence in the Villar de Cañas syncline (Cuenca) has been revealed by using  
462 high resolution shallow seismic tomographic inversion of first arrival traveltimes. The local tomographic image of the  
463 evaporite sedimentary sequence allows observing undulating structures in the base of the boundary layers. The  
464 tomographic Vp velocity model interpreted with the aid of additional geological and geophysical observations, such as  
465 Vp measurements from sonic logs and core description from boreholes provided a detailed mapping of the different  
466 lithologies that build up the sedimentary evaporite sequence. Additional constraints coming from sonic and gamma ray



467 logs were proven to be critical in the interpretation of the inverted velocity model, allowing identification of the detailed  
468 features and geological structures at depth. Well logs and surface geology data allowed interpreting the different  
469 lithologies in the seismic image. The constraints used consisted in average  $V_p$  values and  $V_p$  ranges for the different  
470 lithologies identified from the description of the core samples extracted from the boreholes. This provided the basis for  
471 a pseudo-automatic (geophysically-driven) interpretation, where model cells were assigned to a specific lithology  
472 according to the  $V_p$  value of the corresponding node of the mesh. Despite the relatively complex structure and  
473 composition of the target area, the guided interpretation scheme presented in this study results in a very powerful  
474 procedure to extract structural information from velocity models. However, the consistency between the model and  
475 interpretation reduces its effectiveness when trying to resolve areas characterized by a high uncertainty in the guided  
476 interpretation. This is particularly true for the uppermost layers where discrepancies can be accounted for by different  
477 factors including: the irregular distribution of the boreholes and logging information; overlapping  $V_p$  values for  
478 different lithologies/composition; the influence of physical conditions (pressure, temperature, water content). Therefore,  
479 in those areas the direct mapping/correlation between velocity and lithology might not be applicable without the help of  
480 other constraints, e.g. other geophysical parameters that can provide additional information to distinguish specific  
481 lithologies.  
482

#### 483 **Acknowledgments**

484  
485 This work has been supported by projects ref: CGL2014-56548-P, CGL2016-81964-REDE supported by the Spanish  
486 Ministry of Science and Innovation, 2017 SGR 1022 Generalitat de Catalunya and, by ENRESA. The seismic data  
487 recording system that consisted in 10 GEODE (Geometrics) was provided by the GIPP-GFZ Potsdam (Germany). The  
488 acoustic energy used as source was generated by a 250 kg accelerated weight drop provided by the Instituto Superior  
489 Técnico, Univ. Lisbon, (Portugal) and a 90 kg accelerated weight drop provided by the Univ. of Oviedo, (Spain). The  
490 data is located at the data base server from the Institute of Earth Sciences Jaime Almera, ICTJA, CSIC  
491 (<http://geodb.ictja.csic.es/#dades1>) We are very thankful to Dr. Christan Haberland, Dr. J.M. Gonzalez-Cortina and Prof.  
492 J. Pulgar for their interest in the experiment and assistance during the field operations. We would also like to thank the  
493 valuable comments of Dr. Juan Alcalde that significantly improved the final manuscript.



494

495 **References**

496

497 Andara, E., Guillot, E., Carbonell, R., and García-Lobón, J.L.: Constraining reflectivity in crystalline environment by  
498 using multicomponent VSP data. 73rd European Association of Geoscientists and Engineers Conference and  
499 Exhibition: Unconventional Resources and the Role of Technology. Incorporating SPE EUROPEC: 4174-4178,  
500 2011.

501 Andrés, J., Alcalde, J., Ayarza, P., Saura, E., Marzán, I., Martí, D., Catalán, J.R.M., Carbonell, R., Pérez-Estaún, A.,  
502 García-Lobón, and J.L., Rubio, F.M.: Basement structure of the Hontomín CO<sub>2</sub> storage site (Spain) determined  
503 by integration of microgravity and 3-D seismic data. *Solid Earth*, 7 (3): 827-841, doi:10.5194/se-7-827-2016,  
504 2016.

505 Alcalde, J., Marzán, I., Saura, E., Martí, D., Ayarza, P., Juhlin, C., Pérez-Estaún, A., and Carbonell, R.: 3D geological  
506 characterization of the Hontomín CO<sub>2</sub> storage site, Spain: multidisciplinary approach from seismics, well-  
507 logging and regional data. *Tectonophysics*, 627: 6-25, doi: 10.1016/j.tecto.2014.04.025, 2014.

508 Alcalde, J., Martí, D., Juhlin, C., Malehmir, A., Sopher, D., Saura, E., Marzán, I., Ayarza, P., Calahorrano, A., Pérez-  
509 Estaún, A., and Carbonell, R.: 3-D reflection seismic imaging of the Hontomín structure in the basque-cantabrian  
510 Basin (Spain). *Solid Earth*, 4 (2): 481-496, doi: 10.5194/se-4-481-2013, 2013a.

511 Alcalde, J., Martí, D., Calahorrano, A., Marzán, I., Ayarza, P., Carbonell, R., Juhlin, C., and Pérez-Estaún A.: Active  
512 seismic characterization experiments of the Hontomín research facility for geological storage of CO<sub>2</sub>, Spain.  
513 *International Journal of Greenhouse Gas Control*, 19: 785-795, doi: 10.1016/j.ijggc.2013.01.039, 2013b.

514 Alonso-Zarza, A.M., Calvo, J.P., Silva, P.G., and Torres, T.: Cuenca del Tajo. In: *Geología de España*, edited by Vera,  
515 J.A., SGE-IGME, Madrid, 556-561, 2004.

516 Baumann-Wilke, M., Bauer, K., Schovsbo, N.H., and Stiller, M.: P-wave traveltome tomography for a seismic  
517 characterization of black shales at shallow depth on Bornholm, Denmark. *Geophysics*, 77(5): EN53-EN60. doi:  
518 10.1190/geo2011-0326.1, 2012.

519 Benz, H., Chouet, B., Dawson, P., Lahr, J., Page, R., and Hole, J.: Three dimensional P-and S-wave velocity structure of  
520 Redoubt Volcano, Alaska. *Journal of Geophysical Research*, 101: 8111–8128, doi: 10.1029/95JB03046, 1996.

521 Bergman, B., Tryggvason, A., and Juhlin, C.: High resolution seismic traveltome tomography incorporating static  
522 corrections applied to a till covered bedrock environment. *Geophysics*, 69(4): 1082-1090, doi:  
523 10.1190/1.1778250, 2004.

524 Bergman, B., Tryggvason, A., and Juhlin, C.: Seismic tomography studies of cover thickness and near-surface bedrock  
525 velocities. *Geophysics*, 71(6): U77-U84, doi: 10.1190/1.2345191, 2006.

526 Bernal, I., Tavera, H., Sulla, W., Arredondo, L., and Oyola, J.: Geomorphology Characterization of Ica Basin and Its  
527 Influence on the Dynamic Response of Soils for Urban Seismic Hazards in Ica, Peru, *International Journal of*  
528 *Geophysics*, vol. 2018, Article ID 9434251, 12 pages. Doi:10.1155/2018/9434251, 2018.

529 Biete, C., Roca, E., and Hernáiz-Huerta, P.P.: The Alpine structure of the basement beneath the southern Loranca Basin  
530 and its influence in the thin-skinned contractional deformation of the overlying Mesozoic and Cenozoic cover.  
531 *Geo-Temas*, 13, 173, 2012.

532 Bryś, K., Bryś, T., Ara-Sayegh, M., and Ojrzyńska, H.: Subsurface shallow depth soil layers thermal potential for  
533 ground heat pumps in Poland, *Energy and Buildings*, Volume 165: 64-75, doi: 10.1016/j.enbuild.2018.01.015,  
534 2018.

535 Carbonell, R., Pérez-Estaún A., Maitínez-Landa, L., Martí, D., and Carretero, G.: Geophysical and geological  
536 characterization of fractures within a granitic pluton. *Near Surface Geophysics*, 8 (3): 181-193, doi:  
537 10.3997/1873-0604.2010002, 2010.

538 Carmichael, R. S.: *Practical handbook of physical properties of rocks and minerals*: CRC Press, Inc., 1989.

539 Davis, T. L., Terrell, M. J., Benson, R.D., Cardona, R., Kendall, R.R., and Winarsky, R.: Multicomponent seismic  
540 characterization and monitoring of the CO<sub>2</sub> flood at Weyburn Field, Saskatchewan, *The Leading Edge*, 22(7):  
541 696-697, doi: 10.1190/1.1599699, 2003.

542 De Vicente, G., and Muñoz-Martín, A.: The Madrid Basin and the Central system: A tectonostratigraphic analysis from  
543 2D seismic lines, *Tectonophysics* 602: 259-285, doi: 10.1016/j.tecto.2012.04.003, 2013.

544 Diaz-Molina, M.: Geometry and lateral accretion patterns in meander loops: examples from the Upper Oligocene-  
545 Lower Miocene, Loranca Basin, Spain: in Marzo, M., and Puigdefabregas, P., eds., *Alluvial Sedimentation*:  
546 *International Association of Sedimentologists*, Special Publication 17: 115-131, 1993.

547 Diaz-Molina, M. and Muñoz-García, M.B.: Sedimentary facies and three-dimensional reconstructions of upper  
548 Oligocene meander belts from the Loranca Basin, Spain, *AAPG Bulletin*, V. 94, No. 2: 241-257,  
549 doi:10.1306/07210909010, 2010.

550 Díaz Molina, M., and Tortosa, A.: Fluvial fans of the Loranca Basin, Late-Oligocene-Early Miocene, central Spain. In:  
551 *Tertiary Basins of Spain*, edited by Friend, P., and Dabrio, C., Cambridge University Press, 300-307, 1996.



- 552 Escavy, J.I, Herrero, M.J., and Arribas, M.E.: Gypsum resources of Spain: Temporal and spatial distribution. *Ore*  
553 *Geology Reviews*, Volume 49: 72-84, doi: 10.1016/j.oregeorev.2012.09.001, 2012.
- 554 Escuder-Viruete, J., Carbonell, R., Pérez-Soba, C., Martí, D., and Pérez-Estaún A.: Geological, geophysical and  
555 geochemical structure of a fault zone developed in granitic rocks: Implications for fault zone modeling in 3-D.  
556 *International Journal of Earth Sciences*, 93 (2): 172-188, doi: 10.1007/s00531-003-0378-z, 2004.
- 557 Escuder Viruete, J., Carbonell, R., Martí, D., Jurado, M.J., and Pérez-Estaún A.: Architecture of fault zones determined  
558 from outcrop, cores, 3-D seismic tomography and geostatistical modeling: Example from the Albalá Granitic  
559 Pluton, SW Iberian Variscan Massif. *Tectonophysics*, 361 (1-2): 97-120, doi: 10.1016/S0040-1951(02)00586-3,  
560 2003.
- 561 Festa, V., Tripaldi, S., Siniscalchi, A., Acquafredda, P., Fiore, A., Mele, D., and Romano, G.: Geoelectrical resistivity  
562 variations and lithological composition in coastal gypsum rocks: A case study from the Lesina Marina area  
563 (Apulia, southern Italy). *Engineering Geology*, Volume 202: 163-175, doi: 10.1016/j.enggeo.2015.12.026, 2016.
- 564 Flecha, I., Carbonell, R., Zeyen, H., Martí, D., Palomeras, I., Simancas, F., and Pérez-Estaún A.: Imaging granitic  
565 plutons along the IBERSEIS profile. *Tectonophysics*, 420 (1-2): 37-47, doi: 10.1016/j.tecto.2006.01.019, 2006.
- 566 Flecha, I., Martí, D., Carbonell, R., Escuder-Viruete, J., and Pérez-Estaún A.: Imaging low-velocity anomalies with the  
567 aid of seismic tomography. *Tectonophysics*, 388: 225-238, doi: 10.1016/j.tecto.2004.04.031, 2004.
- 568 Giese, R., Hennings, J., Lüth, S., Morozova, D., Schmidt-Hattenberger, C., Würdemann, H., Zimmer, M., Cosma, C.,  
569 Juhlin, C., and CO2SINK Group: Monitoring at the CO2SINK Site: A Concept Integrating Geophysics,  
570 Geochemistry and Microbiology. *Energy Procedia*, Vol. 1, Issue 1: 2251-2259, doi:  
571 10.1016/j.egypro.2009.01.293, 2009.
- 572 Guimerà, J., De Vicente, G. and Rodríguez-Pascua, M.A.: La Rama Castellano-valenciana. In: *Geología de España*  
573 (Vera, J.A., eds.). Sociedad Geológica Española e Instituto Geológico y Minero de España, pp. 610-612, 2004.
- 574 Guimerà, L., Rivero, R., Salas, A., Casas: Moho depth inferred from gravity and topography in an intraplate area (Iberian  
575 Chain), *Tectonophysics*, Volume 666: 134-143, doi: 10.1016/j.tecto.2015.10.021, 2016.
- 576 Guinea, A., Playà, E., Rivero, L., Himi, M., Bosch, R.: Geoelectrical classification of gypsum rocks. *Surveys*  
577 *Geophysics*. 31 (6): 557-580, doi: 10.1007/s10712-010-9107-x, 2010
- 578 Heincke, B., Günther, T., Dalsegg, E., Rønning, J.S., Ganerød, G.V., and Elvebakk, H.: Combined three-dimensional  
579 electric and seismic tomography study on the Åknes rockslide in western Norway, *Journal of Applied*  
580 *Geophysics*, 70: 292-306, doi: 10.1016/j.jappgeo.2009.12.004, 2010.
- 581 Hole, J.A.: Non-linear high-resolution three-dimensional seismic traveltimes tomography. *Journal of Geophysical*  
582 *Research*, 97: 6553-6562, doi: 10.1029/92JB00235, 1992.
- 583 Hole, J.A., and Zelt, C.: 3D finite differences reflection traveltimes. *Geophysics*, 121:427-434, doi: 10.1111/j.1365-  
584 246X.1995.tb05723.x, 1995.
- 585 IAEA: Storage of Radioactive Waste Safety Guide IAEA Safety Standards Series No. WS-G-6.1 0608-Waste  
586 repositories STI/PUB/1254; (ISBN:92-0-106706-2); 55 pp., 2006.
- 587 Juhlin, C., Giese, R., Zinck-Jorgensen, K., Cosma, C., Kazemeini, H., Juhojuntti, N., Luth, S., Norden, B., and Förster,  
588 A.: 3D baseline seismics at Ketzin, Germany: the CO2SINK project. *Geophysics*, Vol. 72, No.5: B121-B132.  
589 Doi: 10.1190/1.2754667, 2007.
- 590 Kaufmann G., and Romanov D.: Geophysical observations and structural models of two shallow caves in  
591 gypsum/anhydrite-bearing rocks in Germany Geological Society, London, Special Publications, 466, 6, doi:  
592 10.1144/SP466.13. 2017.
- 593 Kazemeini, H., Juhlin, C., and Fomel, S.: Monitoring CO2 response on surface seismic data; a rock physics and  
594 seismic modeling feasibility study at the CO2 sequestration site, Ketzin Germany. *Journal of Applied*  
595 *Geophysics*, Volume 71, Issue 4: 109-124, doi: 10.1016/j.jappgeo.2010.05.004, 2010.
- 596 Kim, J.S., Kwon, S.K., Sanchez, M. and Cho, G.C.: Geological Storage of High Level Nuclear Waste. *KSCE Journal*  
597 *Civil Engineering* 15: 721. doi: 10.1007/s12205-011-0012-8, 2011.
- 598 Kissling, E.: Geotomography with local earthquakes. *Review Geophysics* 26: 659-698, doi:  
599 10.1029/RG026i004p00659, 1988.
- 600 Kissling, E., Ellsworth, W.L., Eberhart-Phillips, D., and Kradolfer, U.: Initial reference models in local earthquake  
601 tomography. *Journal Geophysical Research*, 99, 19635-19646, doi: 10.1029/93JB03138, 1994.
- 602 Letort, J., Roux, P., Vandemeulebrouck, J., Coutant, O., Cros, E., Wathelet, M., Cardellini, C., and Avino, R.: High-  
603 resolution shallow seismic tomography of a hydrothermal area: application to the Solfatara, Pozzuoli,  
604 *Geophysical Journal International*, Volume 189, Issue 3:1725 1733, doi: 10.1111/j.1365-246X.2012.05451.x,  
605 2012.
- 606 Lévêque, J.J, Rivera, L., and Wittlinger, G.: On the use of the checker-board test to assess the resolution of  
607 tomographic inversions. *Geophysical Journal International*, 115: 313-318, doi: 10.1111/j.1365-  
608 246X.1993.tb05605.x, 1993.
- 609 Malehmir, A., Schmelzbach, C., Bongajum, E., Bellefleur, G., Juhlin, C., and Tryggvason, A.: 3D constraints on a  
610 possible deep >2.5 km massive sulphide mineralization from 2D crooked-line seismic reflection data in the  
611 Kristineberg mining area, northern Sweden, *Tectonophysics*, Volume 479, Issues 3-4: 223-240, doi:



- 612 10.1016/j.tecto.2009.08.013, 2009.
- 613 Malehmir, M., Tryggvason, A., Lickorish, H., and Weihed, P.: Regional structural profiles in the western part of the  
614 Palaeoproterozoic Skellefte Ore District, northern Sweden, Precambrian Research, Volume 159, Issues 1–2: 1–  
615 18, doi: 10.1016/j.precamres.2007.04.011, 2007.
- 616 Malehmir, A., Dahlin, P., Lundberg, E., Juhlin, C., Sjöström, H., and Högdahl, K.: Reflection seismic investigations in  
617 the Dannemora area, central Sweden: Insights into the geometry of polyphase deformation zones and magnetite-  
618 skarn deposits, Journal Geophysical Research., 116: B11307, doi: 10.1029/2011JB008643, 2011.
- 619 Martí, D., Carbonell, R., Escuder-Viruete, J., and Pérez-Estaún A.: Characterization of a fractured granitic pluton: P-  
620 and Swaves' seismic tomography and uncertainty analysis. Tectonophysics, 422 (1-4): 99-114, doi:  
621 10.1016/j.tecto.2006.05.012, 2006.
- 622 Martí D., Carbonell, R.R., Tryggvason, A., Escuder, J., and Pérez-Estaún, A.: Calibrating 3D tomograms of a granitic  
623 pluton. Geophysical Research Letters, 29 (17): 15-1-15-4, doi: 10.1029/2001GL012942, 2002a.
- 624 Martí, D., Carbonell, R., Tryggvason, A., Escuder, J., and Pérez-Estaún A.: Mapping brittle fracture zones in three  
625 dimensions: High resolution travelttime seismic tomography in a granitic pluton. Geophysical Journal  
626 International, 149 (1):95-105, doi: 10.1046/j.1365-246X.2002.01615.x, 2002b.
- 627 Martí, D., Carbonell, R., Flecha, I., Palomeras, I., Font-Capó, J., Vázquez-Suñé, E., Pérez-Estaún, A.: High-resolution  
628 seismic characterization in an urban area: Subway tunnel construction in Barcelona, Spain Geophysics, Vol. 73,  
629 No. 2: B41-B50, doi: 10.1190/1.2832626, 2008.
- 630 Martinius, A.W., Geel, C.R., and Arribas, J.: Lithofacies characterization of fluvial sandstones from outcrop gamma-ray  
631 logs (Loranca Basin, Spain): the influence of provenance. Petroleum Geoscience, 8: 51-62, 1, doi:  
632 10.1144/petgeo.8.1.51, 2002.
- 633 Muñoz-Martin, A., and De Vicente, G.: Cuantificación del acortamiento alpino y estructura en profundidad del extremo  
634 sur-occidental de la Cordillera Ibérica (Sierras de Altomira y Bascañana), Revista Sociedad Geológica de  
635 España, 11(3-4): 233-252, 1998.
- 636 Novitsky, C. G., Holbrook, W.S., Carr, B.J., Pasquet, S., Okaya, D. and Flinchum, B.A.: Mapping Inherited Fractures  
637 in the Critical Zone using Seismic Anisotropy from Circular Surveys. Geophysical Research Letters, 45. doi:  
638 10.1002/2017GL075976, 2018.
- 639 Ogaya, X., Alcalde, J., Marzán, I., Ledo, J., Queralt, P., Marcuello, A., Martí, D., Saura, E., Carbonell, R., and  
640 Benjumea, B.: Joint interpretation of magnetotelluric, seismic, and well-log data in Hontomán (Spain). Solid  
641 Earth, 7 (3): 943-958. doi:10.5194/se-7-943-2016, 2016.
- 642 Paige, C.C., and Saunders, A.: LSQR: An algorithm for sparse linear equations and sparse least squares. ACM  
643 Transactions on Mathematics Software, 8: 43-71, doi: 10.1145/355984.355989, 1982.
- 644 Place, J., Malehmir, A., Högdahl, K., Juhlin, C., and Persson Nilson, K.: Seismic characterization of the Grängesberg  
645 iron deposit and its mining-induced structures, central Sweden, Interpretation 3(3): SY41-SY56, doi:  
646 10.1190/INT-2014-0212.1, 2015.
- 647 Piña-Varas, P., Ledo, J., Queralt, P., Roca, E., García-Lobón, J.L., Ibarra, P., and Biete, C.: Two-dimensional  
648 magnetotelluric characterization of the El Hito Anticline (Loranca Basin, Spain), Journal of Applied Geophysics,  
649 Volume 95:121-134, doi: 10.1016/j.jappgeo.2013.06.002, 2013.
- 650 Rawlinson, N., and Spakman, W.: On the use of sensitivity test in seismic tomography. Geophysical Journal  
651 International 205: 1221–1243 doi: 10.1093/gji/ggw084, 2016.
- 652 Samyn, K., Travelletti, J., Bitri, A., Grandjean, G., and Malet, J.P.: Characterization of a landslide geometry using 3D  
653 seismic refraction travelttime tomography, Journal of Applied Geophysics, 86:120-132, doi:  
654 10.1016/j.jappgeo.2012.07.014, 2012.
- 655 Seillé, H., Salas, R., Pous, J., Guimerà, J., Gallart, J., Torne, M., Romero-Ruiz, I., Diaz, J., Ruiz, M. Carbonell, R., and  
656 Mas, R.: Crustal structure of an intraplate thrust belt: The Iberian Chain revealed by wide-angle seismic,  
657 magnetotelluric soundings and gravity data, Tectonophysics, Volume 663: 339-353 doi:  
658 10.1016/j.tecto.2015.08.027, 2015.
- 659 Sopena, A., and De Vicente, G.: Cordilleras Ibérica y Costero-Catalana, 5.1. Rasgos generales In: Geología de España,  
660 edited by Vera, J.A., SGE-IGME, Madrid, 467-470, 2004.
- 661 Steeples, D.W: Engineering and environmental geophysics at the millenium. Geophysics, 66(1): 31-35, doi:  
662 10.1190/1.1444910, 2001.
- 663 Tryggvason, A., Rognvaldsson, S.T. & Flovenz, O.G.: Three-dimensional imaging of the P- and S-wave velocity  
664 structure and earthquake locations beneath Southwest Iceland. Geophysal Journal International, 151: 848–866,  
665 doi: 10.1046/j.1365-246X.2002.01812.x, 2002.
- 666 Tryggvason, A. and Bergman, B.: A travelttime reciprocity discrepancy in he Podvin and Lecomte time3d finite  
667 difference algorithm. Geophysical Journal International, 165: 432-435, doi: 10.1111/j.1365-246X.2006.02925.x,  
668 2006.
- 669 Ugalde, A., Villaseñor, A., Gaité, B., Casquero, S., Martí, D., Calahorrano, A., Marzán, I., Carbonell, R., and Pérez-  
670 Estaún, A.: Passive seismic monitoring of an experimental CO2 geological storage site in Hontomín (Northern  
671 Spain) Seismological Research Letters, 84 (1), 75-84, doi: 10.1785/0220110137, 2013.



- 672 Vegas, R., Vazquez, J.T., Suriñach, E., and Marcos, A.: Model of distributed deformation, block rotations and crustal  
673 thickening for the formation of the Spanish Central System. *Tectonophysics*, 184, 367–378, doi: 10.1016/0040-  
674 1951(90)90449-I, 1990.
- 675 Vidale, J.: Finite-difference calculation of traveltimes. *Bulletin of the Seismological Society of America*, 78 (6), 2062–  
676 2076, 1988.
- 677 Wadas, S. H., Tanner, D.C, Polom, U., and Krawczyk, C.M.: [Structural analysis of S-wave seismics around an urban  
678 sinkhole: evidence of enhanced dissolution in a strike-slip fault zone. \*Natural Hazards and Earth System  
679 Sciences\*, 17: 2335-2350.](#) doi: 10.5194/nhess-17-2335-2017, 2017.
- 680 Witherspoon, P.A. Cook, N.G., Gale, JE: Gale Geologic storage of radioactive waste: field studies in Sweden. *Science*,  
681 Vol. 211, Issue 4485: 894-900, doi: 10.1126/science.7466363, 1981.
- 682 Yao, Z.S., , Roberts, R.G., and Tryggvason, A.: Calculating resolution and covariance matrices for seismic tomography  
683 with the LSQR method, *Geophysical Journal International*, Volume 138, Issue 3: 886–894, doi: 10.1046/j.1365-  
684 246x.1999.00925.x, 1999.
- 685 Yordkayhun, S., Juhlin, C., Giese, R., Cosma, C.: Shallow velocity-depth model using first arrival traveltimes inversion  
686 at the CO2SINK site, Ketzin, Germany. *Journal of Applied Geophysics*, Vol. 63: 68-79.  
687 doi:10.1016/j.jappgeo.2007.05.001, 2007.
- 688 Yordkayhun S., Juhlin C., and Norden B.: 3D seismic reflection surveying at the CO2SINK project site, Ketzin,  
689 Germany: A study for extracting shallow subsurface information. *Near Surface Geophysics*, Vol. 7, No. 2: 75-91,  
690 doi: 10.3997/1873-0604.2008036 , 2009a.
- 691 Yordkayhun, S., Tryggvason, A., Norden, B., Juhlin, C., and Bergmann, B: 3D seismic traveltimes tomography imaging  
692 of the shallow subsurface at the CO2SINK project site, Ketzin, Germany. *Geophysics* Vol. 74, No. 1: G1-G15,  
693 doi: 10.1190/?1.3026553, 2009b.
- 694 Zelt, C., Azaria, A., and Levander, A: 3D seismic refraction traveltimes tomography at a groundwater contamination  
695 site. *Geophysics*, 71(5): H67-H78, doi: 10.1190/1.2258094, 2006.
- 696

## 697 Figure Captions

698

699 Figure 1. (a). Simplified geological map of the Iberian Range in eastern Iberian peninsula, with the location of the study  
700 area marked in black box, (modified from Guimerà et al. (2004). (b) Local geological map of the Villar de Cañas  
701 syncline. The target area is marked by a blue rectangle. The 2D seismic reflection profiles acquired in this experiment  
702 are also located in the map. (c) Detailed stratigraphic columns describing the main units observed in both flanks of the  
703 syncline.

704

705 Figure 2. Geometry of the acquisition experiment. Red dots are position of the source, white dots are the position of the  
706 receivers. Receivers consisted in single vertical component exploration geophones connected to an array of 10 GEODE  
707 (Geometrics) data acquisition system. Light blue dots indicate drilled boreholes. Weight drop (250 kg) used (from the  
708 Inst. Superior Tecnico Lisbon, Portugal)

709

710 Figure 3. Example of shot gather recorded by the array of 10 GEODES, 24 channels each. The red ticks indicate the  
711 traveltimes picks of the first arrivals used as inputs for the tomographic inversion.

712

713 Figure 4. (a) 3D Seismic compressional wave velocity model ( $V_p$ ) derived from the over 500.000 traveltimes picks of  
714 the first arrivals in the shot gathers. The velocity range goes from nearly 900 m/s (reds) to over 4500 m/s (blues). (b)  
715 Comparison between the smoothly resampled  $V_p$  log derived from the sonic at borehole SVC-6 (light blue) and the  
716 vertical  $V_p$  profile extracted from the block at the location of the SVC-6 indicated by a black arrow in the block. The re-  
717 sampling of the log was carried out so that it would be comparable to the grid size used for the parametrization of the  
718 velocity model which in this case is of 10x10x5m.

719

720 Figure 5. Checker-board tests, synthetic recovery test taking into account the real acquisition geometry on a model  
721 involving velocity anomalies of dimensions 75x50x25m, approximately. Checker-board analysis is a conventional  
722 scheme to assess the resolution of the tomographic inversion approaches [Leveque et al., 1993; Rawlinson et al.,  
723 20154]. (a) Corresponds to a cross-section of the input synthetic velocity model consisting of box anomalies. (b)  
724 Corresponds to a cross-section across the recovered velocity model. The best resolution is between 25 and 75 m. depth.  
725 (c) Corresponds to a depth slice (map view) across the input model showing the synthetic velocity anomalies (squares).  
726 (d) Corresponds to a depth slice across the recovered velocity model at a 50 m depth. (e) Is the acquisition geometry, the  
727 red line near the top corresponds to the location of the depth section of (a) . In the cross sections and depth slices red  
728 corresponds to low seismic velocity and blue to high values of the seismic velocities.

729

730 Figure 6. Drill-holes in the target area with the borehole geophysical logs used in this study. This reveals the correlation



731 between the rock samples, its description and the values of the physical properties, Gama ray (GR), sonic logs (Vp).  
732 The top part of the figure reveals the logging data with the correlation between the available boreholes. The bottom  
733 table defines the summary criterion used for the interpretation of the different lithologies. The Vp value should be  
734 representative of the corresponding lithologies. This criterion is used later in the text to differentiate between the  
735 different lithologies in the velocity cube obtained from the tomographic inversion. The left box illustrated the location  
736 of the boreholes within the acquisition geometry of the seismic survey, with the outcropping geology of the target area.  
737

738

739 Figure 7. Velocity model grid of the shallow subsurface, it has been color coded according to the lithologies indicated in  
740 the included scale/table which is the one derived in Figure 6. LT, Lutites; Ytr the gypsum-lutite transition layer; Y1 and  
741 Y2, Gypsum units.

742

743 Figure 8, 3D Volume representations of the different lithologic units. LT, Lutites; Ytr the gypsum-lutite transition layer;  
744 Y1 and Y2, Gypsum units.

745

746 Figure 9. Resulting shallow subsurface structure represented as detailed cross-sections. Cross-sections integrate the  
747 velocity model derived from the tomography, the constraints provided by the boreholes and the extrapolation of surface  
748 geology data (in discontinuous drafted lines). Four different east-west and north-south cross-sections are showed with  
749 their locations within the study area. Note that towards the east (in the geological map), the Ytr outcrops at surface, as  
750 well as the Y unit. This reveals that the entire layered sequence dips to the west.

751

752

753

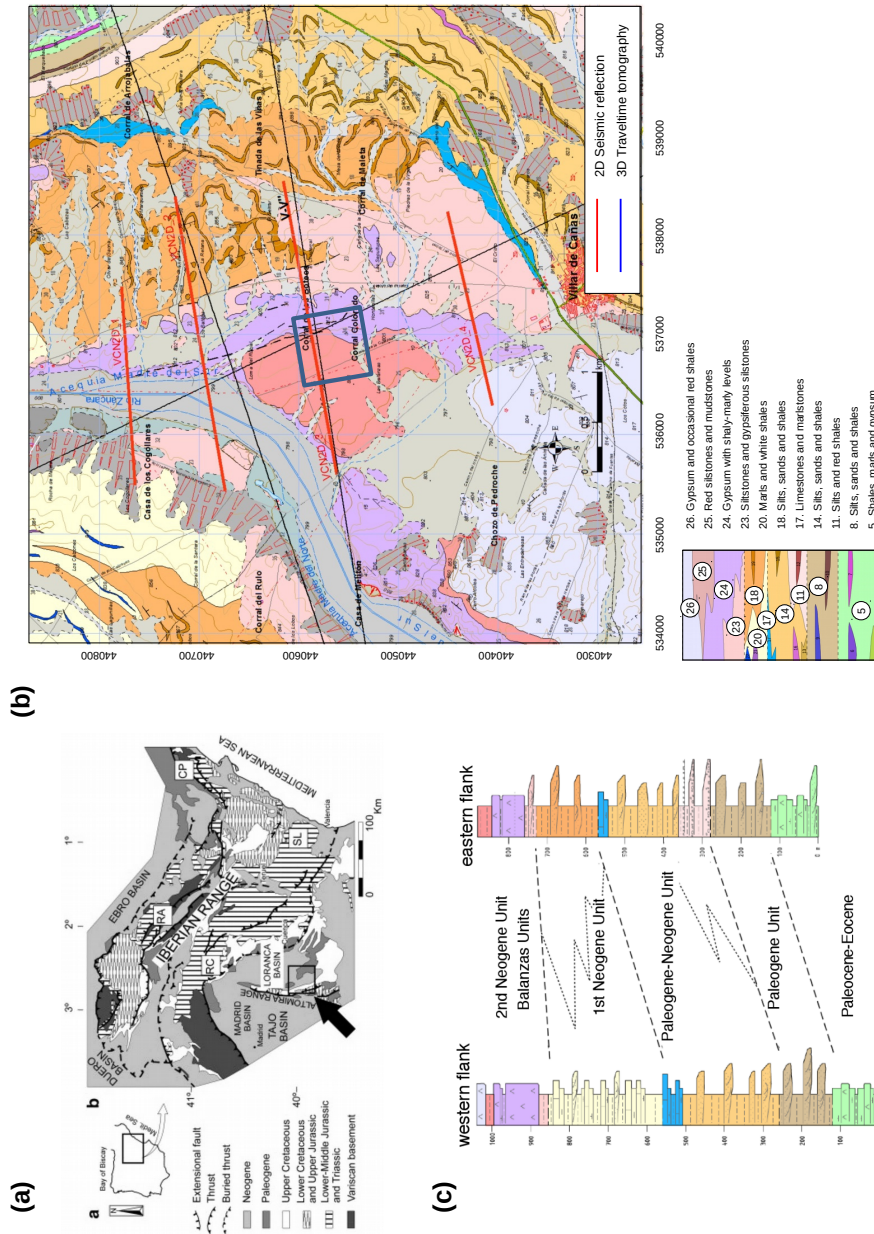


Fig. 1

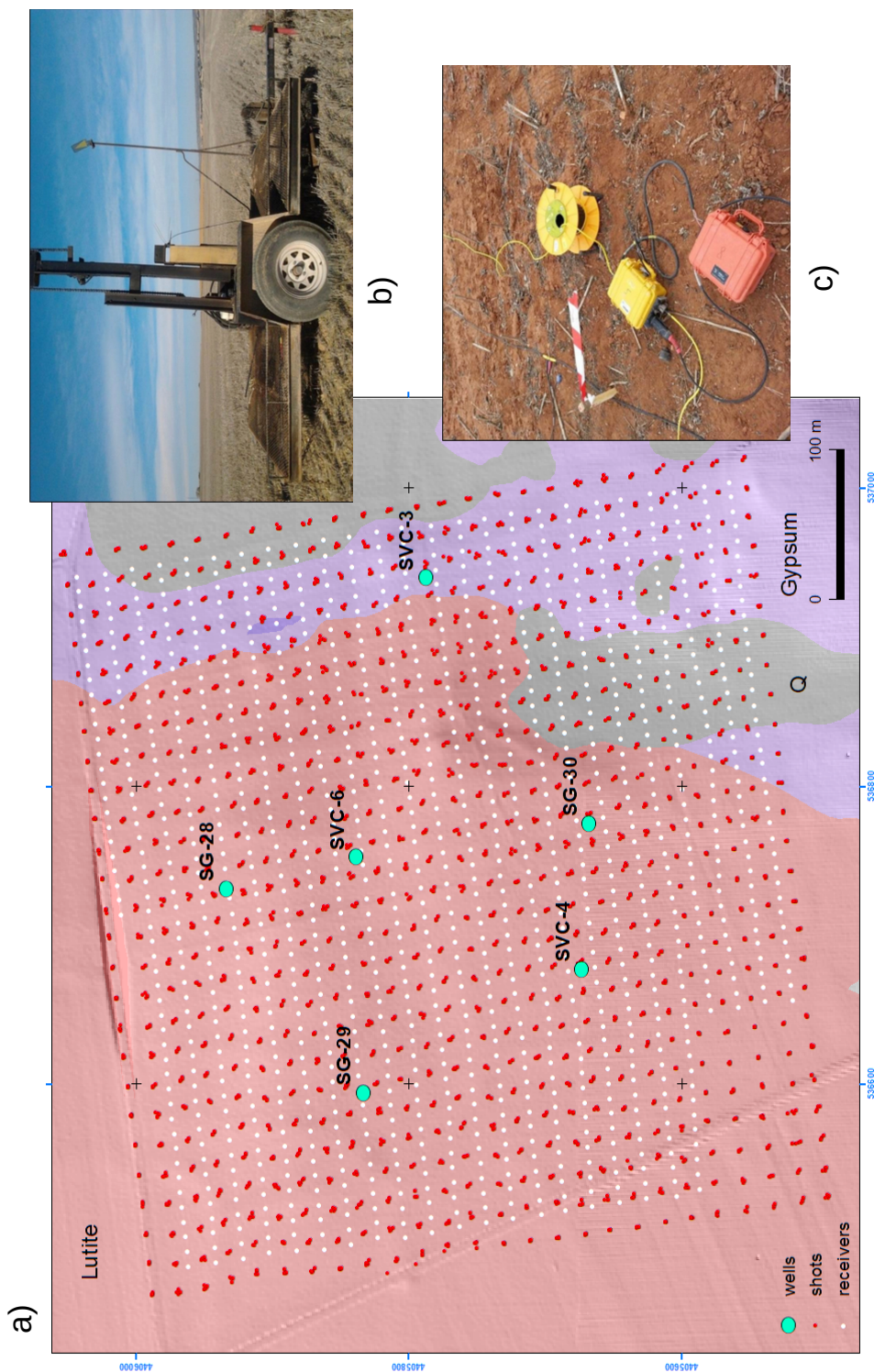


Fig. 2

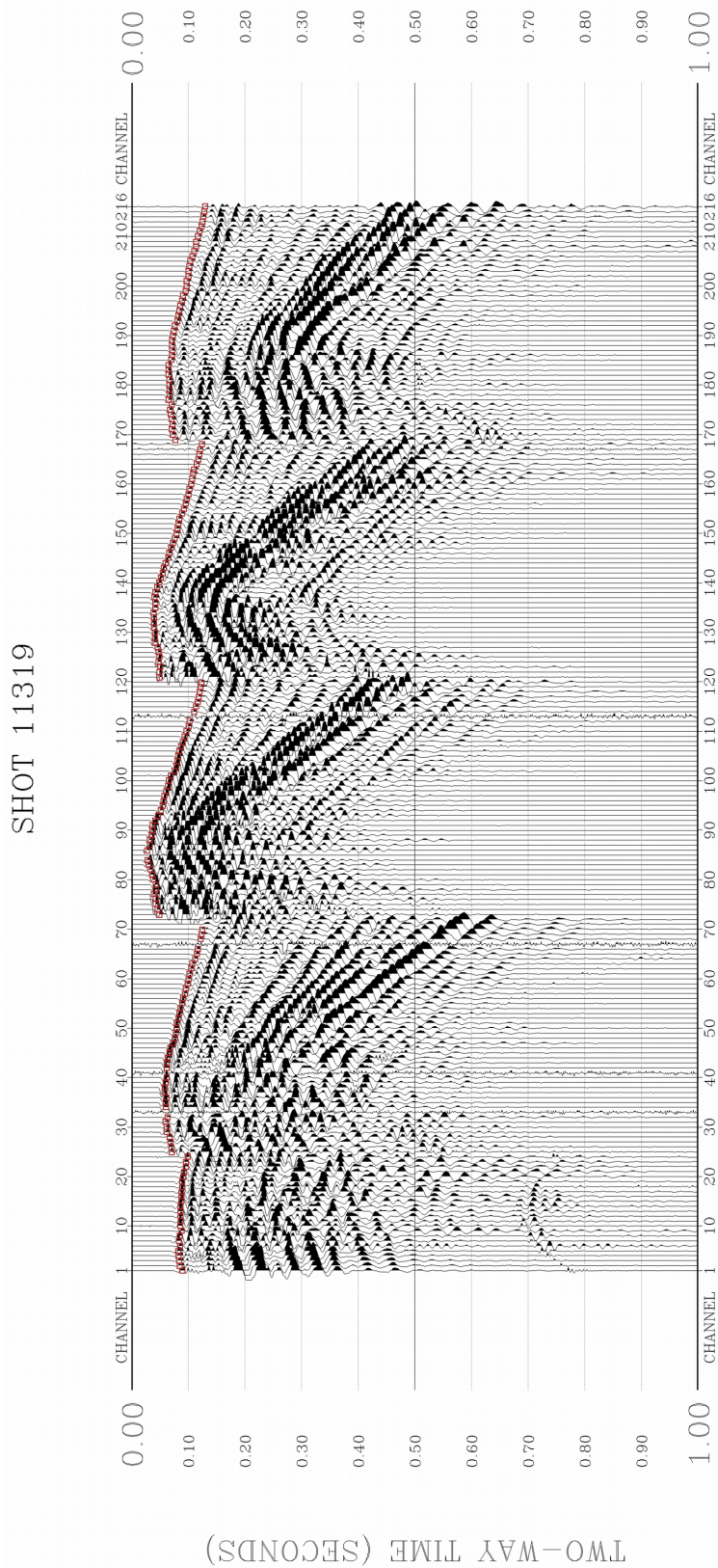


Fig. 3

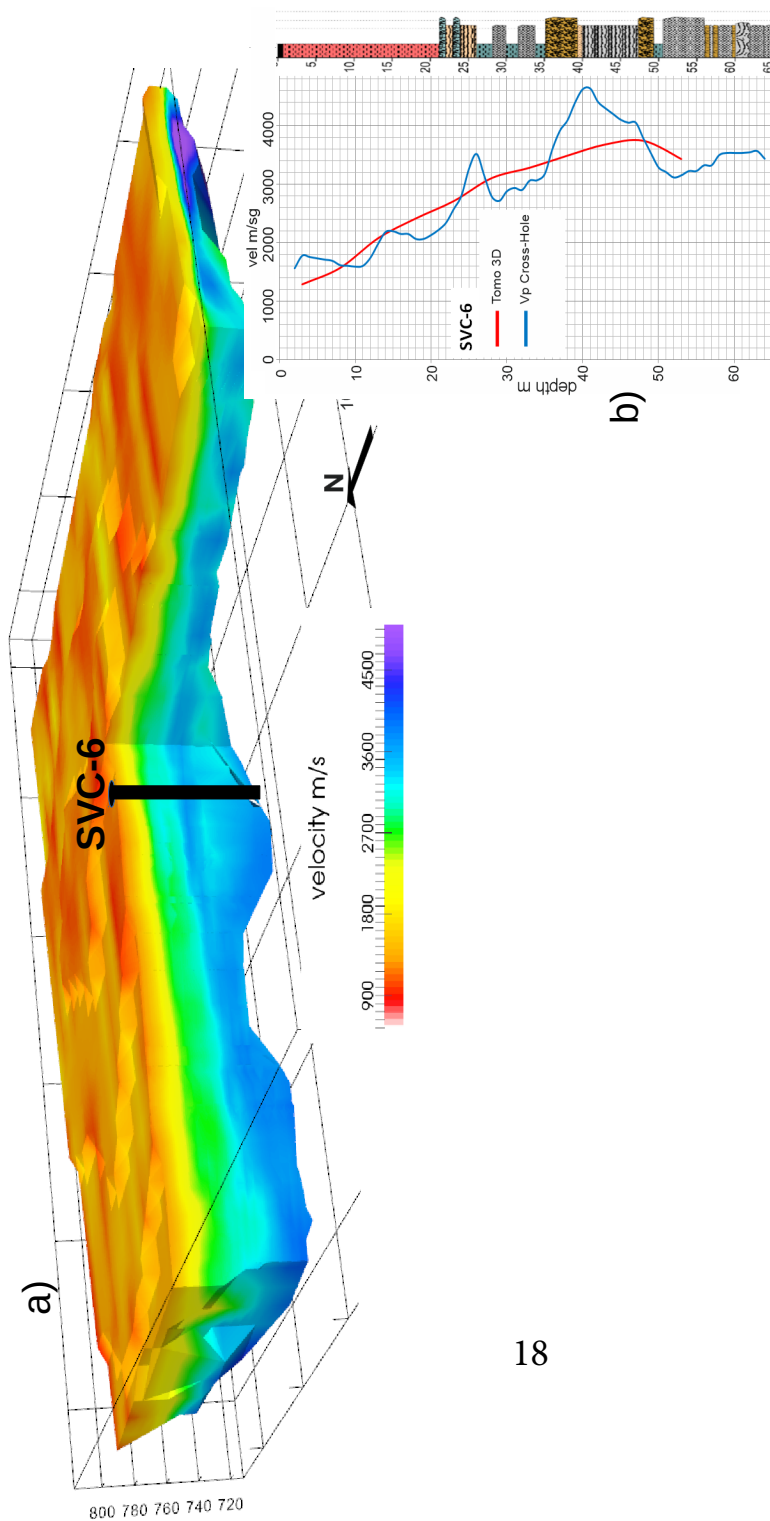


Fig. 4

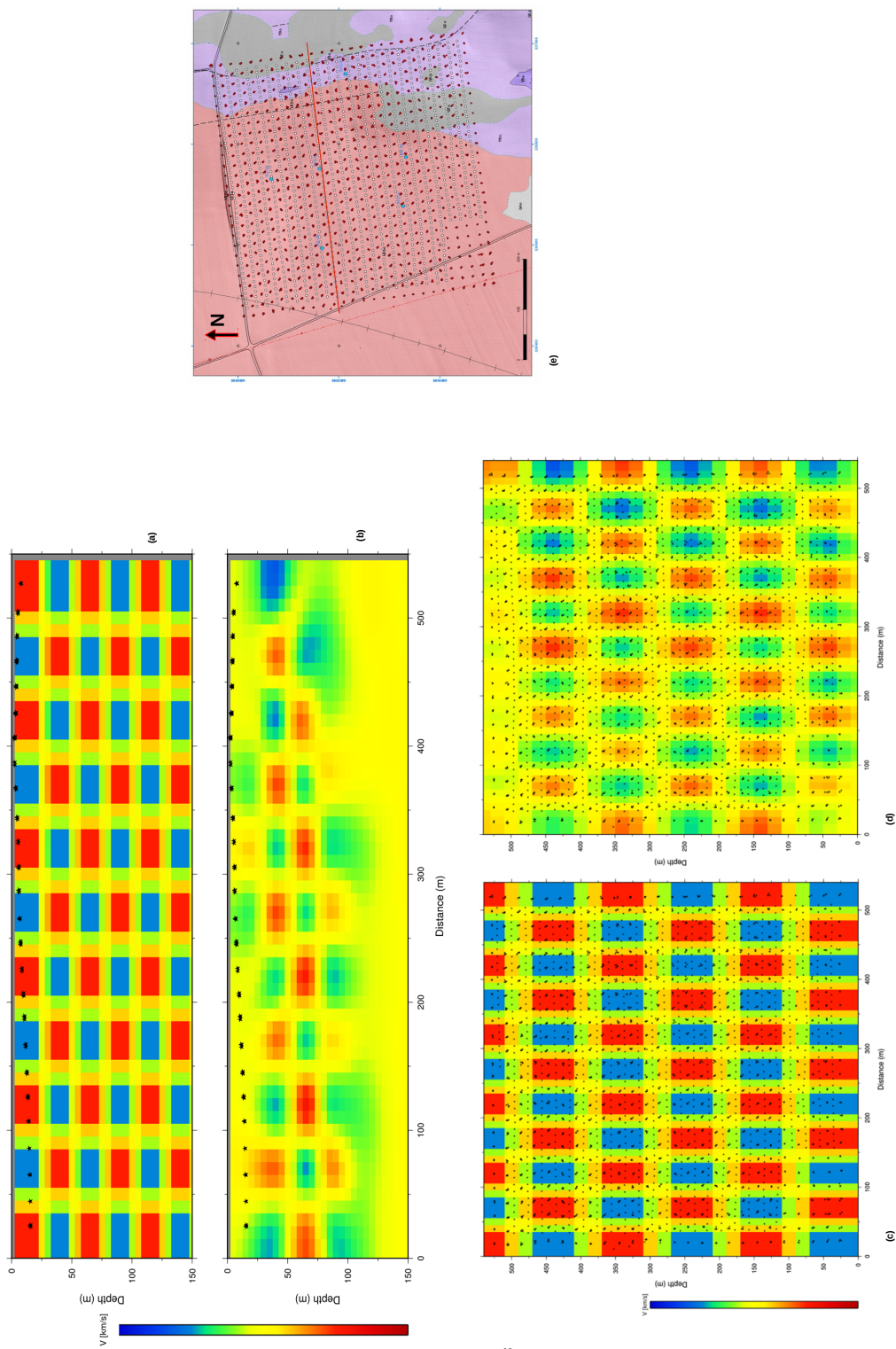


Fig. 5

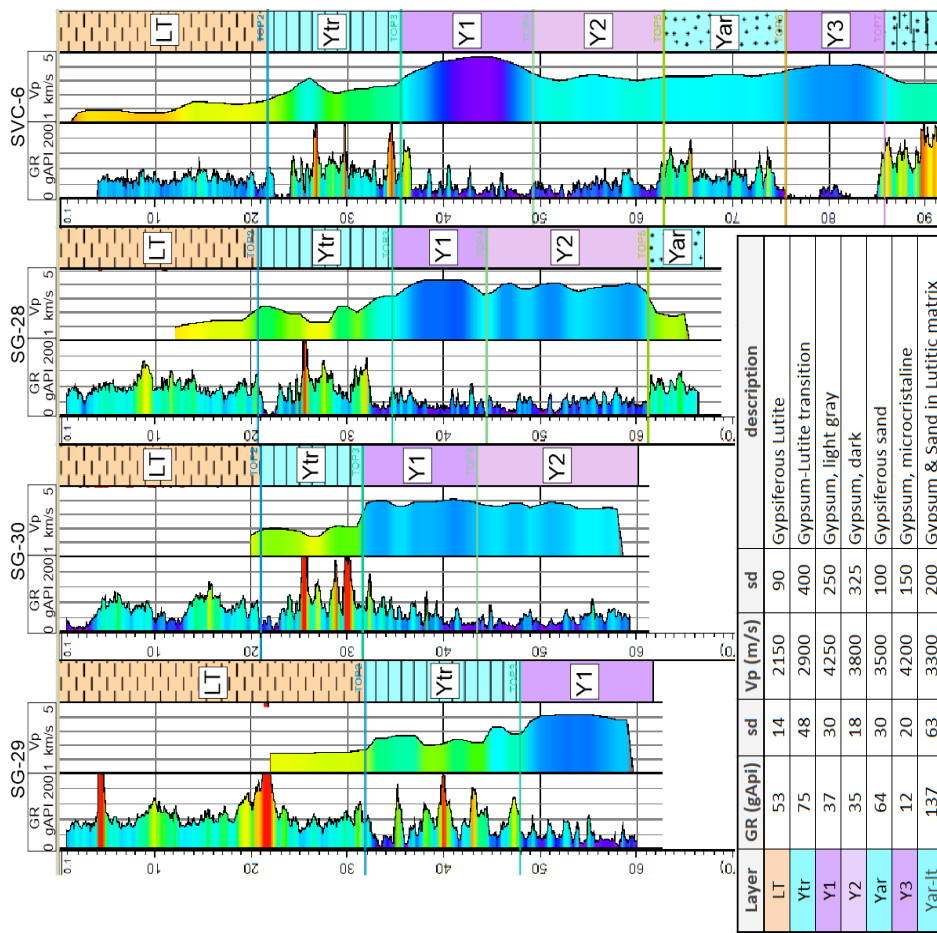


Fig. 6

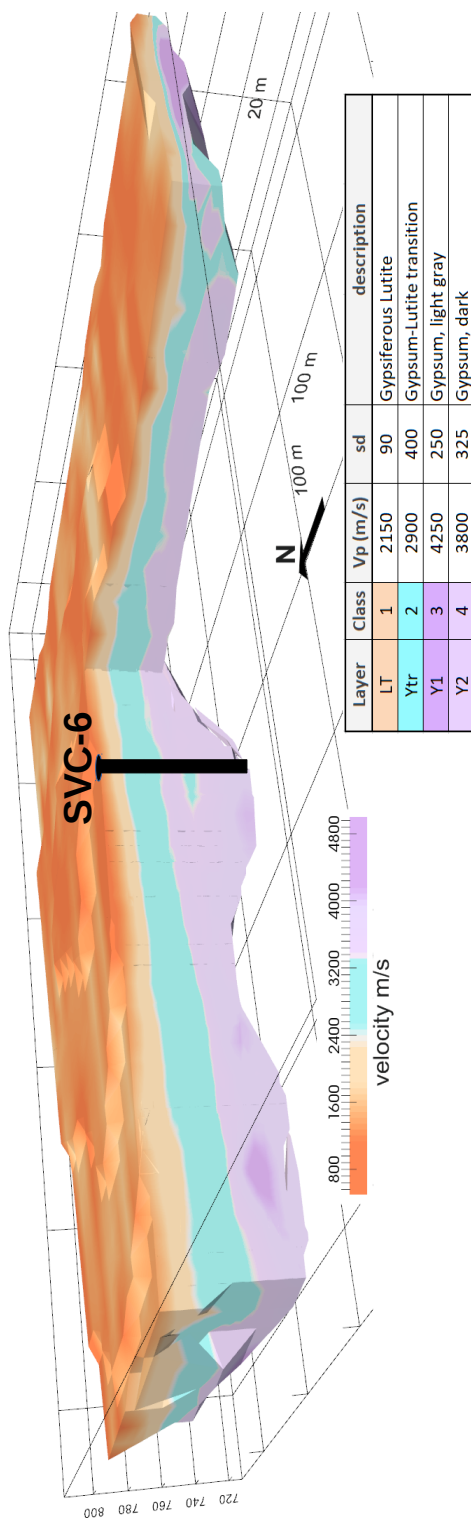


Fig. 7

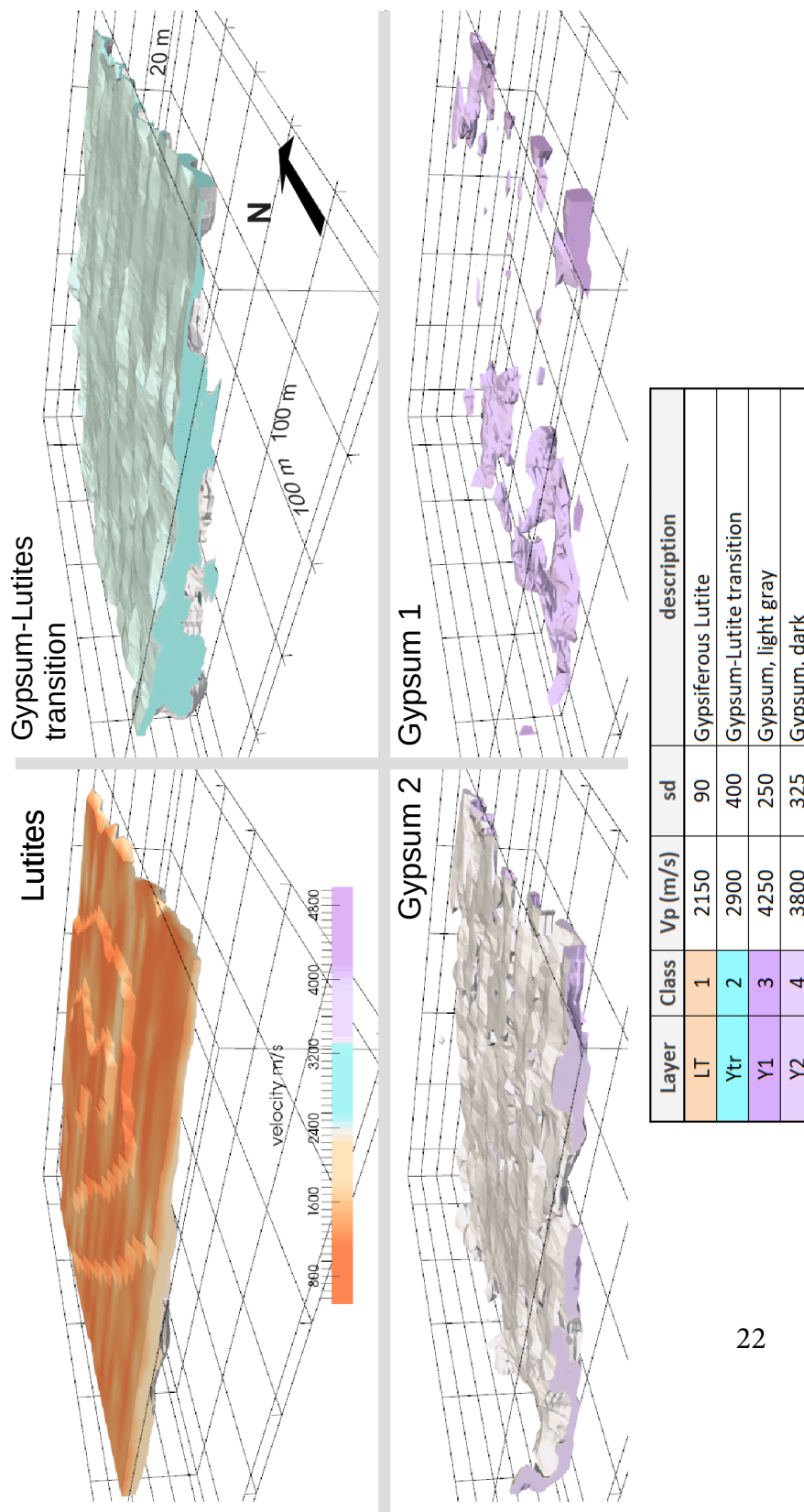


Fig. 8

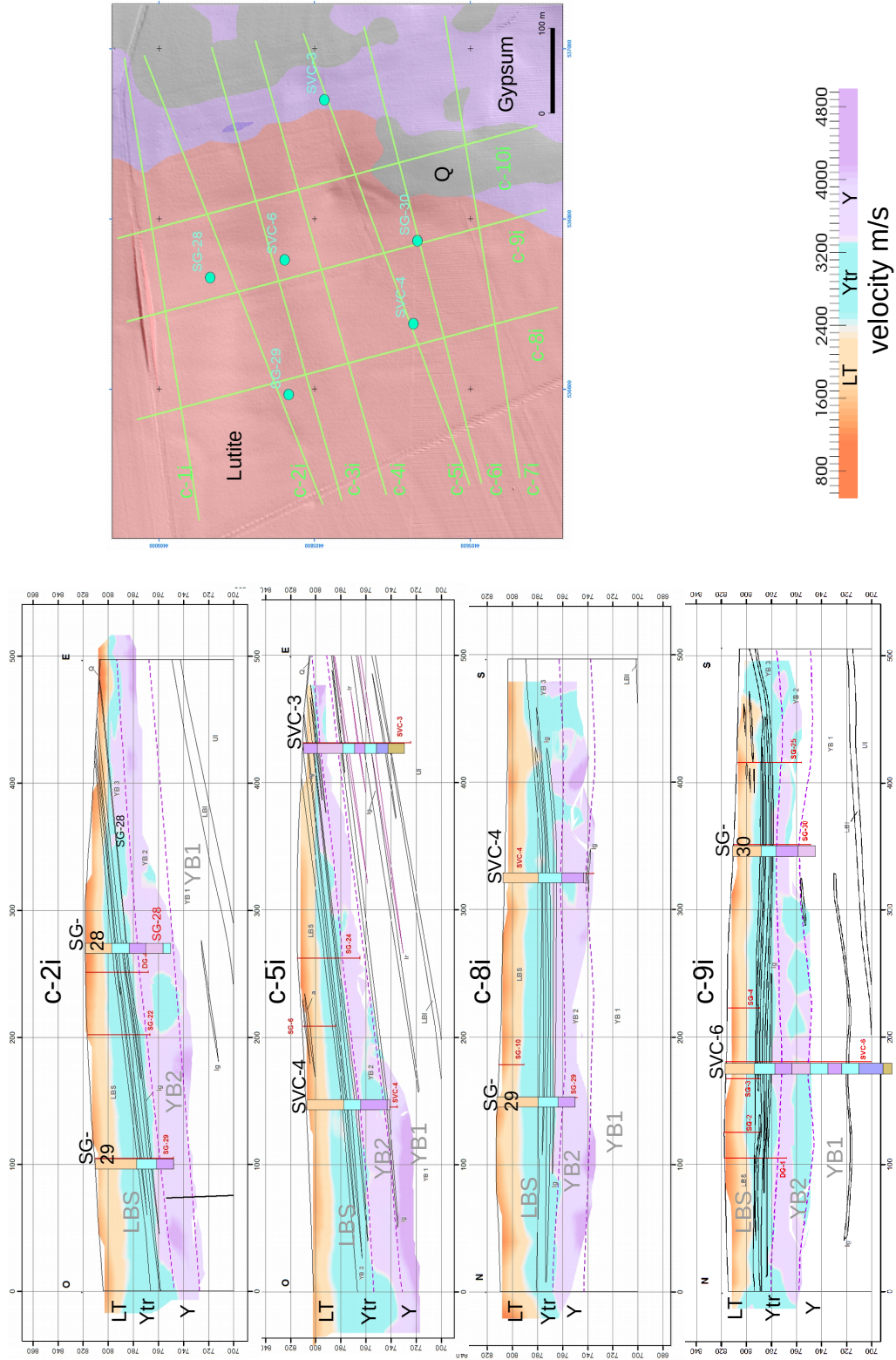


Fig. 9